Ultrafast electron dynamics of graphene quantum dots: High harmonic generation

Suresh Gnawali ⬤, Rupesh Ghimire, Krishna Rana Magar, Sayed Jaber Hossaini, and Vadym Apalkov
Department of Physics and Astronomy, Georgia State University, Atlanta, Georgia 30303, USA

We study theoretically nonlinear optical properties of graphene quantum dots placed in a field of a short and strong linearly polarized optical pulse. We address the problem of high harmonic generation in quantum dots and how such nonlinear effect is affected by dephasing processes in a quantum dot. The dephasing makes the ultrafast electron dynamics more irreversible with a large residual population of the excited quantum dot levels. In relation to the high-harmonic spectrum, with increasing the dephasing time, the intensities of the low-frequency harmonics increase while the cutoff energy decreases. The dependence of the cutoff energy on the amplitude of the optical pulse is also sensitive to the frequency of the pulse. When the frequency of the optical pulse is much less than the quantum dot band gap, this dependence is almost linear, but when the frequency of the pulse is comparable to the band gap, the cutoff energy shows saturation behavior at large field amplitude, >0.4 V/Å.

I. INTRODUCTION

Strong optical pulses, the amplitudes of which are comparable to internal electric fields in solids, are intensively used to probe and control both the transport and optical properties of electron systems [1–14]. The electron dynamics in such pulses is highly nonlinear, which results in such nonlinear optical effects as nonlinear absorption and high harmonic generation (HHG) [15]. HHG has a special role since it allows one to convert a low-frequency pulse in the visible or infrared range into the high-frequency radiation, for example, extreme ultraviolet or soft x rays [16–24]. The mechanism, which is responsible for generation of high frequency harmonics, is different for a system of randomly positioned atoms and a system of a crystalline solid. HHG in atomic or molecular gases occurs through a three-step process which consists of a tunnel ionization of an electron, its acceleration in the laser field, and a subsequent recollision with an atom [25]. Such a process results in unique linear dependence of the HHG cutoff on the energy of the pulse [16].

In solids, the HHG occurs through the combination of two types of dynamics induced by the field of the pulse: interband and intraband dynamics [19–21,26–28]. Due to the interband dynamics, the electrons are redistributed between the bands of a solid, while, due to the intraband dynamics, the electrons are transferred through the nonparabolic bands, which results in nonlinear optical response. Both of these dynamics contribute to the generation of high harmonics. Which dynamics provides the main contribution depends on the band gap of a solid and the parameters of the pulse, e.g., its frequency. The unique property of HHG in solids is that the HHG energy cutoff has linear dependence on the pulse amplitude [19], while in gases, the HHG cutoff has linear dependence on the pulse intensity [16].

HHG is one of the characteristics of the nonlinear optical response of solids. Their nonlinear optical properties strongly depend on the band structure, impurity level, and other internal characteristics of solids. For example, tin sulphide (SnS) has shown excellent nonlinear optical properties due to a tunable band gap and fast carrier mobility [29], a system consisting of a few layers of bismuthene has shown strong nonlinear refraction effects and all-optical switching [30], graphdiyne has demonstrated relatively large nonlinear refractive index [31]. A family of two dimensional (2D) materials, 2D transition metal carbides or nitrides (MXenes), has shown promising nonlinear optical properties, which can be tuned by varying the ratios of M or X elements and their surface terminations [32].

Nonlinear optical properties of solids can also be tuned by changing their dimensionality, making them two-dimensional, one-dimensional, or zero-dimensional systems. Zero-dimensional systems, which are called quantum dots (QDs) or artificial atoms [33,34], consist of a finite number of atoms of the corresponding solid. The QDs have many applications in different fields of science [35–39]. Due to dimensional quantization, the energy spectra of QDs are discrete, which is similar to spectra of regular atoms. At the same time, the QDs still have the features of the crystal structure of the corresponding solid, namely, within the region of a QD, the atoms are placed periodically and the discrete energy levels of the QD can usually be identified as belonging to different bands of the solid. Thus, the HHG spectra of QDs can resemble the ones of the corresponding solids. In Ref. [40], a transformation of the HHG spectrum from the atomic one to the spectrum of the crystalline solid is traced within the one-dimensional model. It was shown that such a transformation occurs for the QD consisting of just six nuclei.

In the present paper, we consider HHG in QDs, which are based on graphene [41–44]. Graphene is a monolayer of carbon atoms with a honeycomb crystal structure [45,46]. It has unique transport and optical properties, which are related to its specific relativistic low-energy dispersion of the Dirac
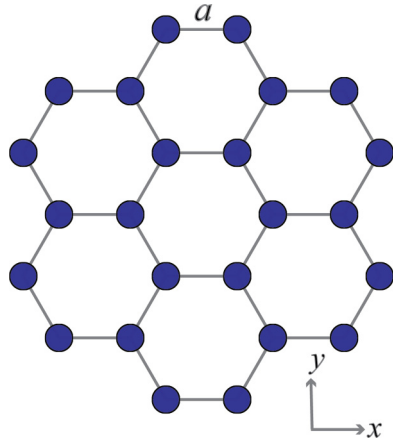
FIG. 1. Graphene quantum dot consisting of 24 carbon atoms. The incident laser pulse is linearly polarized along the *x* direction. The distance between the nearest-neighbor atoms is $a = 1.42$ Å.

type [47–50]. In a strong field of an ultrashort optical pulse, such dispersion results in interference patterns in the conduction band (CB) population distribution in the reciprocal space [51]. In graphene with broken inversion symmetry, an ultrashort circularly polarized optical pulse results in ultrafast valley polarization [52], which occurs due to the valley dependent topological resonance [11,52]. Graphene QDs, interacting with a short optical pulse, have also shown nonlinear absorption properties [53]. The nonlinear absorption of other monolayer QD systems, transition-metal dichalcogenide QDs, has been also reported in Ref. [54]. Such nonlinear optical response has been studied for ultrashort pulses, the duration of which is much less than the characteristic dephasing or relaxation time. In this case, the electron dynamics during the pulse is coherent. In the present paper, we address the problem of a finite relaxation rate and study how the relaxation processes can modify graphene QD's nonlinear optical response, such as HHG. It has been previously shown that the HHG is sensitive to the relaxation rate in three-dimensional solids [28].

The relaxation processes result in noncoherent electron dynamics in the field of the pulse. Such dynamics is described within the density matrix approach [55,56], which is used below in the present paper. We also consider only the internal electron dynamics within the QD region without taking into account the possibility of ionization of the QD.

The paper is organized as follows. In Sec. II, we introduce the model and main equations. In Sec. III, we discuss the results, which are summarized in the concluding Sec. IV.

II. MODEL AND MAIN EQUATIONS

We consider a graphene QD which consists of $N = 24$ carbon atoms, see Fig. 1. The distance between the nearest-neighbor atoms is $a = 1.42$ Å. The electron system of such a QD is described within the tight-binding model with the Hamiltonian of the following form:

$$H_0 = -t \sum_{<ij>} (\hat{a}_i^\dagger \hat{a}_j + \text{H.c.}), \tag{1}$$

where i and j label the sites of QD, $\hat{a}_i^\dagger$ and $\hat{a}_i$ are creation and annihilation operators for an electron on site i, and $t = -3.03$ eV is the hopping integral [57,58]. For the QD consisting of N atoms, the tight-binding model gives N levels with the wave functions ψ_n and the corresponding energies E_n, where $n = 1, \ldots N$. Here the $N/2$ lowest energy levels belong to the valence band (VB), while all other levels belong to the CB. Below we assume that, in the initial state, i.e., before the pulse, the VB states are occupied and the CB states are empty.

The graphene QD placed in an external electron field of an optical pulse is described by the following time-dependent Hamiltonian:

$$H(t) = H_0 + H'(t). \tag{2}$$

Here the Hamiltonian $H'(t)$ describes the interaction of electrons with the field of the pulse,

$$H'(t) = -e \sum_i \hat{a}_i^\dagger \hat{a}_i \mathbf{r}_i \cdot \mathbf{F}(t), \tag{3}$$

where $\mathbf{F}(t)$ is the time-dependent electric field of the pulse and $\mathbf{r}_i$ is the position of the ith atom. We consider a pulse that is linearly polarized in the x direction, see Fig. 1, with the electric field of the following form:

$$F_x(t) = F_0 e^{-(t/\tau_0)^2} \cos(\omega_0 t), \tag{4}$$

where ω_0 is the frequency of the pulse and τ_0 is the duration of the pulse. Below we consider three frequencies of the pulse, $\hbar\omega_0 = 1$ eV, 2 eV, and 3.1 eV, with parameter τ_0 equal to 10 fs. In this case, there are at least eight oscillations of the field of the pulse.

To include the relaxation processes, we describe the electron system within the density matrix approach. Without relaxation, the time evolution of the density operator, $\hat{\rho}$, is determined by the following equation:

$$\frac{d\hat{\rho}}{dt} = \frac{i}{\hbar}[\hat{\rho}, H] = \frac{i}{\hbar}[\hat{\rho}, H_0] + \frac{i}{\hbar}[\hat{\rho}, H'], \tag{5}$$

where $[\hat{A}, \hat{B}]$ is the commutator of operators $\hat{A}$ and $\hat{B}$. The above Eq. (5) describes the coherent electron dynamics and is equivalent to the time-dependent Schrödinger equation with Hamiltonian $H(t)$.

Taking the matrix elements of the left- and right-hand sides of Eq. (5) between the states ψ_n of field-free Hamiltonian H_0, we obtain the following matrix equation:

$$\dot{\rho}_{mn} = i\omega_{mn}\rho_{mn} + \frac{i}{\hbar} \sum_k (\rho_{mk} H'_{kn} - H'_{mk}\rho_{kn}), \tag{6}$$

where $\omega_{mn} = \frac{(E_n - E_m)}{\hbar}$, E_n is the energy corresponding to the state ψ_n, $\rho_{mn} = <\psi_m|\hat{\rho}|\psi_n>$, $H'_{kn} = -e < \psi_k|x|\psi_n > F_x(t)$, and $D_{x,kn} = e < \psi_k|\hat{x}|\psi_n >$ is the dipole matrix element of the dipole operator $e\hat{x}$.

Introducing the density matrix in the interaction representation,

$$\tilde{\rho}_{mn} = \rho_{mn} e^{-i\omega_{mn}t}, \tag{7}$$

we rewrite Eq. (6) in the following form:

$$\dot{\tilde{\rho}}_{mn} = \frac{i}{\hbar} \sum_k \left[\tilde{\rho}_{mk} e^{i\omega_{nk}t} H'_{kn} - H'_{mk}\tilde{\rho}_{kn} e^{i\omega_{km}t} \right]. \tag{8}$$

Equation (8) describes the coherent electron dynamics in the field of the pulse, which does not take into account the relaxation effects. The relaxation processes affect both the diagonal elements of the density matrix and the nondiagonal elements. The relaxation of the diagonal elements is related to the interlevel transitions, while the relaxation of the nondiagonal elements determines the coherence of the electron dynamics. The loss of the coherence occurs at a much faster rate than the rate of the interlevel transitions. Below we consider only the relaxation of the nondiagonal elements of the density matrix with the characteristic relaxation (dephasing) time τ. Thus, Eq. (8) does not change for $m = n$, while for $m \neq n$ it becomes

$$\dot{\tilde{\rho}}_{mn} = \frac{i}{\hbar} \sum_k \left[\tilde{\rho}_{mk} e^{i\omega_{nk}t} H'_{kn} - H'_{mk} \tilde{\rho}_{kn} e^{i\omega_{km}t} \right] - \frac{\tilde{\rho}_{mn}}{\tau}. \quad (9)$$

We solve the system of differential Eqs. (8) and (9) numerically using the ODEINT library, which is a collection of different numerical algorithms to solve initial value problems of ordinary differential equations [59]. The initial conditions are that, before the pulse, all the VB states are occupied and all the CB states are empty, i.e., $\tilde{\rho}_{nn} = 1$ if $n \in$ VB and $\tilde{\rho}_{nn} = 0$ if $n \in$ CB.

With the known density matrix, we can calculate the CB population N_{CB} using the following expression:

$$N_{CB}(t) = \sum_{m \in CB} \tilde{\rho}_{mm}(t). \quad (10)$$

Here the sum is over all QD CB states.

The dipole moment, which is used to find the induced radiation of the QD, is given by the following expression:

$$d_x(t) = \sum_{mn} \tilde{\rho}_{mn}(t) e^{i\omega_{mn}t} D_{x,nm}. \quad (11)$$

Then, the total radiated power at frequency ω is determined by the Fourier transform of the time derivative of the dipole moment, $\mathcal{F}_\omega[\dot{d}_x]$, namely, the radiated power is given by the following expression:

$$P(\omega) = \frac{\mu_0 \omega^2}{12\pi c} |\mathcal{F}_\omega[\dot{d}_x]|^2. \quad (12)$$

Below we consider the normalized power, P_N, defined by the following expression:

$$P_N(\omega) = \frac{P(\omega)}{P(\omega_0)}. \quad (13)$$

The order of the high harmonic is also defined in units of ω_0:

$$N_\omega = \frac{\omega}{\omega_0}. \quad (14)$$

III. RESULTS AND DISCUSSIONS

We consider a graphene QD, the structure of which is shown in Fig. 1. It consists of 24 carbon atoms and has D_{6h} symmetry. The energy spectrum of such a QD is obtained within the tight-binding model and consists of singly, doubly, and triply degenerate levels. The corresponding energy spectrum is shown in Fig. 2. Twelve levels with the negative energies are initially occupied and belong to the VB. The levels with the positive energies belong to the CB. The band gap for the QD is 3 eV. The maximum energy difference between
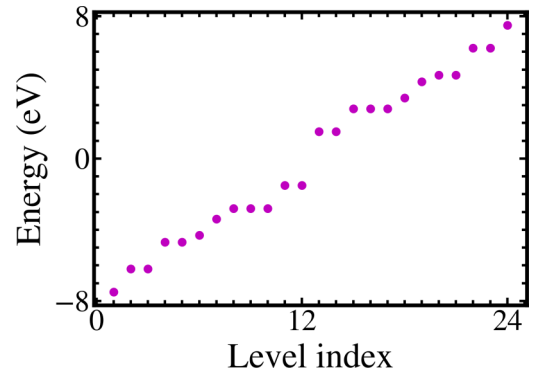
FIG. 2. Energy spectrum of graphene QD shown in Fig. 1. The spectrum consists of singly, doubly, and triply degenerate levels. Levels with the negative energy correspond to the valence band while the levels with the positive energy correspond to the conduction band. Before the pulse, all valence band levels are occupied.

the CB and the VB levels is around 16 eV. In this case, if the high harmonics are generated through transitions between QD levels, then 16 eV should be the maximum frequency that can be generated in such a QD. The time variations of populations of QD levels, i.e., dressing of the QD states due to electron-pulse interactions, result in harmonics with the frequencies larger than 16 eV, as discussed below.

We consider graphene QDs of a small size only, i.e., a QD with 24 atoms. Such QD has a relatively large band gap, 3 eV, so for the optical pulse with a frequency of 1–2 eV there is no resonant transitions within the system. With increasing the QD size, the band gap due to dimensional quantization decreases, resulting in resonant transitions at relatively small frequencies of the pulse. At the same time, the main effects of the relaxation processes on the HHG in graphene QDs are already captured by QDs of a small size.

We apply a linearly polarized pulse, the profile of which is shown in Fig. 3(a) for the field amplitude of $F_0 = 0.5$ V/Å and the pulse frequency of $\hbar\omega_0 = 1$ eV. From the solution of the density matrix equation, we obtain the CB population, see Eq. (10), and the time-dependent dipole moment of the electron system. Their typical time dependencies are shown in Figs. 3(b) and 3(c). The CB population illustrates highly irreversible electron dynamics when the residual CB population, i.e., population after the pulse, is comparable to the maximum CB population during the pulse. The positions of the maxima of N_{CB} are correlated with the maxima of $|F(t)|$.

The typical profile of the dipole moment of QDs is shown in Fig. 3(c). It is roughly proportional to the electric field of the pulse but with some nonlinear features, which finally determine the nonlinear optical response of the system and generation of high harmonics in the radiation spectrum.

The electron dynamics in the field of the optical pulse strongly depends on the relaxation processes. To illustrate such dependence, we show in Fig. 4 the CB population for different relaxation times, τ. The field amplitude is 0.5 V/Å. Here, we consider two frequencies of the pulse, which are both below the band gap of graphene QDs: $\hbar\omega_0 = 1$ eV, which is almost three times less than the QD band gap, and $\hbar\omega_0 = 2$ eV. One of the characteristics of the electron dynamics is its reversibility, i.e., returning the system to its initial state
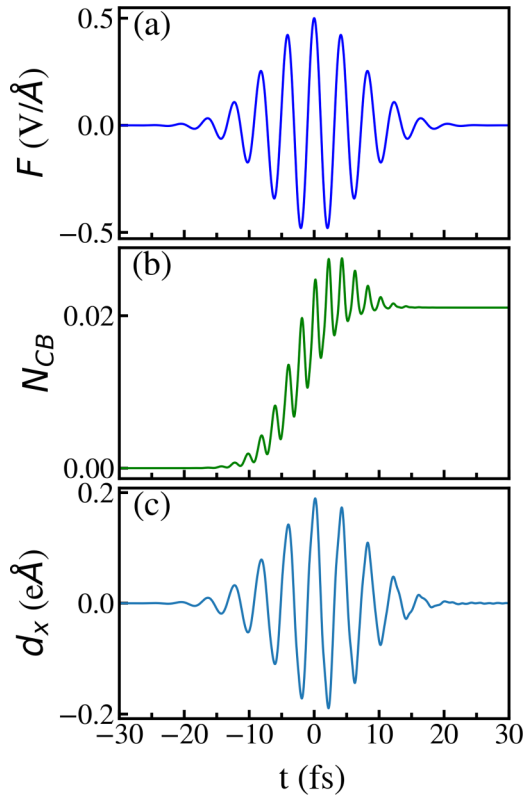
FIG. 3. (a) Profile of a linearly polarized pulse. The pulse amplitude is 0.5 V/Å and the frequency of the pulse is $\hbar\omega_0 = 1$ eV. (b) Conduction band population N_{CB} as a function of time. The QD is in the field of the pulse shown in (a). The conduction band population is normalized by the number of electrons, i.e., it is divided by 12. The corresponding dipole moment is shown in (c). Only x component of the dipole moment is nonzero. The dipole moment roughly follows the profile of the electric field shown in (a).

after the pulse. We introduce quantitative characteristics of the reversibility, η, as the ratio of the CB population after the pulse and the maximum CB population during the pulse:

$$\eta = \frac{N_{CB}^{residual}}{N_{CB}^{max}}. \quad (15)$$
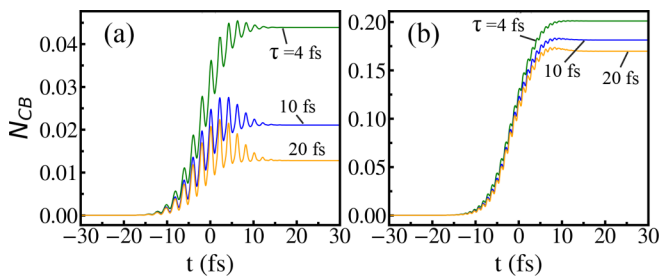
FIG. 4. Conduction band population as a function of time. The conduction band population is normalized by the number of electrons, i.e., it is divided by 12. The corresponding relaxation times are shown next to the lines. The frequency of the pulse is $\hbar\omega_0 = 1$ eV (a) and $\hbar\omega_0 = 2$ eV (b). The pulse amplitude is 0.5 V/Å.
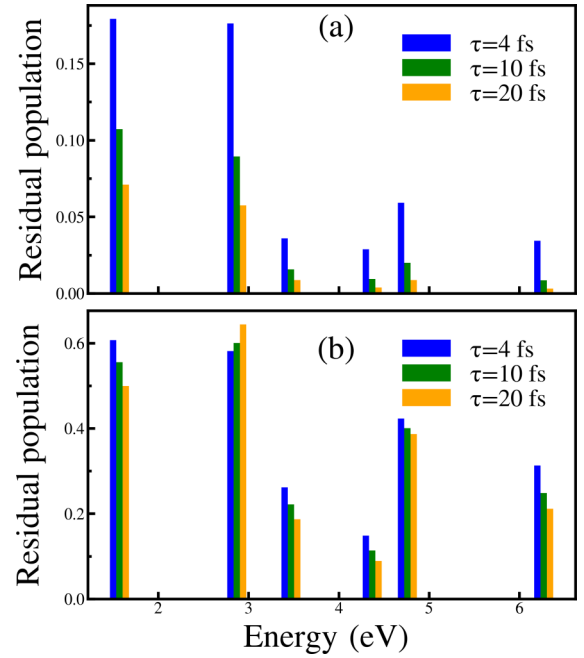
FIG. 5. Residual population of conduction band levels. The pulse amplitude is 0.5 V/Å. The corresponding dephasing times are marked in each panel. The frequency of the pulse is $\hbar\omega_0 = 1$ eV (a) and $\hbar\omega_0 = 2$ eV (b).

The ratio η is between zero and one, where $\eta = 0$ corresponds to a perfectly reversible dynamics, while $\eta = 1$ corresponds to a highly irreversible dynamics.

For small frequency of the pulse, see Fig. 4(a), with increasing the relaxation time, the electron dynamics becomes more reversible. Here, the reversibility parameter η decreases from 0.98 for $\tau = 4$ fs to 0.6 for $\tau = 20$ fs. Thus, for $\tau = 4$ fs, the electron dynamics is highly irreversible, while, for $\tau = 20$ fs, the electron dynamics is partially reversible. Such partial reversibility of the electron dynamics is related to its coherence, which is more preserved for larger values of τ.

A different situation occurs at a larger frequency of the pulse, see Fig. 4(b), where the frequency of the pulse is $\hbar\omega = 2$ eV. In this case, the electron dynamics is much less sensitive to the relaxation time and the dynamics is highly irreversible for all values of τ, see Fig. 4(b). Here, for all cases, the parameter η is close to 0.99. At the same time, the whole CB population is much larger than the CB population for the low frequency case, see Fig. 4(a). For example, for $\hbar\omega_0 = 1$ eV and $\tau = 4$ fs the residual CB population is around 0.04, see Fig. 4(a), while for $\hbar\omega_0 = 2$ eV and $\tau = 4$ fs it is around 0.2, see Fig. 4(b).

The total CB population shown in Fig. 4 describes the net effect of the pulse on the QD. To clarify how different levels of the QD respond to the optical field, we show in Fig. 5 the residual populations of different CB levels. As expected, the levels with lower energies are generally more populated compared to the higher energy levels, but this dependence is not monotonic and some higher energy levels are more populated than the lower energy levels. This is due to properties of the dipole matrix elements, which do not show monotonic dependence on the energy of the levels.
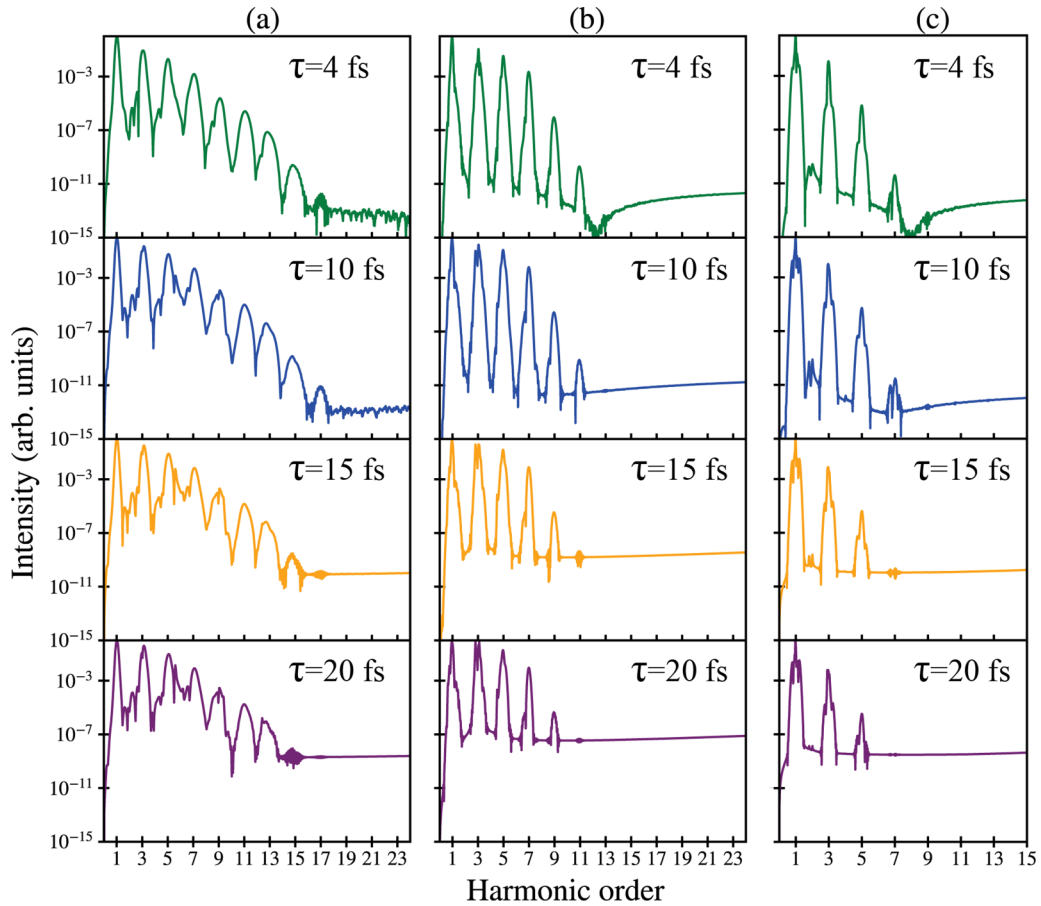
FIG. 6. Emission spectrum of graphene QD. High harmonics with well-defined cutoffs are clearly visible in the spectrum. The corresponding relaxation times are marked for each graph. The frequency of the pulse is $\hbar\omega_0 = 1$ eV in (a), $\hbar\omega_0 = 2$ eV in (b), and $\hbar\omega_0 = 3.1$ eV in (c). With increasing the relaxation time, the emission spectrum becomes more noisy with less defined high harmonic peaks. The pulse amplitude is $F_0 = 0.4$ V/Å.

The dependencies of the populations of individual levels on the relaxation time are sensitive to the frequency of the pulse. For the pulse frequency of 1 eV, see Fig. 5(a), with increasing the relaxation time, the populations of CB levels are suppressed. Such suppression is more pronounced for the higher energy levels. For example, when the relaxation time increases from 4 fs to 20 fs, the population of the lowest CB level decreases by a factor of ≈ 2.5, while the population of the highest energy level decreases by almost 11 times. When the frequency of the pulse becomes close to the band gap, see Fig. 5(b), the populations of the energy levels have weak dependence on the relaxation time. When the relaxation time increases from 4 fs to 20 fs, the populations of the levels change by less than $\approx 20\%$. Also, for all CB levels except one, with increasing the relaxation time, the populations decrease, but for the second CB level we observe a different behavior. For this level, when the frequency of the pulse is 2 eV, with increasing τ, its population slightly increases. This is related to triple degeneracy of the second CB level, see Fig. 2, which results in large density of states associated with this level.

The emission spectra of the QD is calculated from Eq. (12). Since polarization of the pulse is along the axis of symmetry of graphene QD, i.e., along the x axis, there is no induced dipole moment along the y direction and the dipole radiation from the system is linearly polarized along the x direction.

In Fig. 6, we show the radiation spectra for three different frequencies of the pulse and different values of the relaxation time. Here, we added the results for the frequency of $\hbar\omega_0 = 3.1$ eV, which is a little larger than the band gap. We did not study the electron dynamics at this frequency in great detail since, as we can see from Fig. 6, there are only a few high harmonics that are generated in this case, see Fig. 6(c). For example, at the relaxation time of 20 fs, the maximum harmonic that is generated at $\hbar\omega_0 = 3.1$ eV is 5, while at the frequency of 1 eV, it is 13.

Since the QD has an inversion symmetry, only odd harmonics are generated [60]. The radiation spectra have clear cutoff frequencies, which depend both on the relaxation time and the frequency of the pulse, namely, with increasing the frequency of the pulse, the maximum harmonic order that is generated decreases and, with increasing the relaxation time, the cutoff frequency also decreases. Thus, when the electron dynamics becomes incoherent, i.e., at small relaxation times, the system generates more high harmonics, see Fig. 6, compared to the coherent case, $\tau = 20$ fs. Such behavior is correlated with the population of the CB levels shown in Fig. 5, where with increasing τ, the higher energy levels become less populated, which results in suppression of the high harmonics.

Comparing the results for different frequencies of the pulse, see Figs. 6(a)–6(c), we can say that, with increasing the
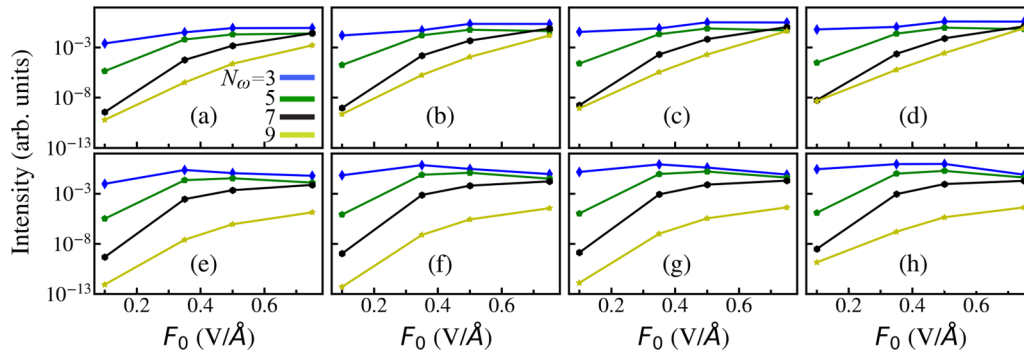
FIG. 7. Intensity of the first four high harmonics ($N_\omega = 3$, 5, 7, and 9) versus the amplitude of the optical pulse, F_0. The frequency of the pulse is $\hbar\omega_0 = 1$ eV in (a)–(d) and 2 eV in (e)–(h). The relaxation time is 4 fs (a), (e); 10 fs (b), (f); 15 fs (c), (g); and 20 fs (d), (h).

frequency of the pulse, the energy cutoff increases. For example, for the relaxation time of $\tau = 4$ fs, the highest harmonic that is generated by the pulse with the frequency of 1 eV [see Fig. 6(a)] is 15 with the corresponding energy of 15 eV. For the same relaxation time, the highest harmonic for the pulse with the frequency of 2 eV [see Fig. 6(b)] is 11, the energy of which is 22 eV. At the same time, when the frequency of the pulse reaches the band gap, see Fig. 6(c), the maximum harmonics is 7 with the corresponding energy of 21.7 eV, which suggests that the energy cutoff reaches a saturated value when the frequency of the pulse approaches the band gap. Similarly, looking at the results for the relaxation time of 20 fs, see Fig. 6, we can find that the maximum energies of the high harmonics are 13 eV, 18 eV, and 15.5 eV, for the pulse frequencies of 1 eV, 2 eV, and 3.1 eV, respectively. In this case, there is even a small suppression of the energy cutoff when the frequency of the pulse becomes close to the band gap.

Thus, the laser pulse with the higher frequency, but below the band gap, strongly perturbs the system, resulting in generation of higher frequency harmonics and higher energy cutoff comparing to the case of the low frequency pulse. Such behavior is correlated with the results shown in Fig. 5, where the populations of the CB levels with high energies are larger for the higher frequency pulse.

Another property of the emission spectra shown in Fig. 6 is that, with decreasing the relaxation time, the emission spectra become less noisy and with well-defined harmonic peaks. For example, for the relaxation time of $\tau = 20$ fs, the emission spectrum between the fifth and seventh harmonics has extra noisy features which disappear at the relaxation time of $\tau = 4$ fs. The reason for such behavior is that, for a shorter relaxation time, fewer trajectories contribute to a given harmonic [61,62], while for a longer relaxation time, multiple trajectories, which occur during the coherent electron dynamics, result in extra interference effects and complex emission spectra [63].

The dependencies of the intensities of high harmonics on the pulse amplitude are shown in Fig. 7 for different relaxation times and different frequencies of the pulse. Only the first four lowest harmonics are shown. When the frequency of the pulse is 1 eV, see Figs. 7(a)–7(d), the intensities of the high harmonics monotonically increase with F_0. With increasing the harmonic order, the dependence of its intensity on F_0

becomes stronger. For example, for $N_\omega = 3$, the intensity has a weak dependence on F_0 and is almost constant at 10^{-3}, while for $N_\omega = 9$, the intensity changes from 10^{-8} at small F_0 to 10^{-3} at large F_0. Such behavior is similar for all relaxation times.

When the frequency of the pulse becomes close to the band gap, see Figs. 7(e)–7(h), where the frequency of the pulse is 2 eV, the intensities of high harmonics become non-monotonic functions of the field amplitude for low harmonics, namely, the intensities of the third and fifth harmonics have maxima at the field amplitude close to 0.4 V/Å. At the same time, the intensities of the higher harmonics, $N_\omega = 7$ and 9, have monotonic dependence on F_0.

Another difference between the low and high frequencies of the pulse is that the ninth harmonic ($N_\omega = 9$) has much smaller intensity for the case of $\hbar\omega_0 = 2$ eV compared to the one of $\hbar\omega_0 = 1$ eV. This is related to the fact that, for the pulse frequency of 2 eV, the ninth harmonics has the energy of 18 eV, which is larger than the maximum range of singe-particle energies within the QD, see Fig. 2, where this range is around 16 eV. As a result, the ninth harmonic is generated due to collective transitions between many levels, which results in its low intensity for the pulse with 2 eV frequency.

To clarify the effect of relaxation time on the radiation spectra, we show in Fig. 8 the intensities of the first four harmonics as functions of the relaxation time. In Figs. 8(a) and 8(e), which correspond to the low-field amplitude of 0.1 V/Å, only the first three harmonics are shown since the fourth harmonics ($N_\omega = 9$) is not generated in this case. For all cases, shown in Fig. 8, the intensities monotonically increase with the relaxation time. Thus, the largest intensities of the high harmonics are realized for the coherent electron dynamics, i.e., for the large relaxation time. The radiation spectra also show a stronger sensitivity to the relaxation processes at small field amplitude, namely, at $F_0 = 0.1$ V/Å, the intensities of the high harmonics change by almost two orders of magnitude when τ increases from 4 fs to 20 fs, see Figs. 8(a) and 8(e), while at $F_0 = 0.75$ V/Å, the corresponding variations of the intensities are ten times smaller, see Figs. 8(d) and 8(h).

The intensities of the high harmonics in Figs. 6–8 are shown in units of the intensity of the main peak at the frequency ω_0. The intensity of the main peak can be estimated from the calculated dipole moment and its Fourier transform. For example, for the field amplitude of 0.5 V/Å, the frequency
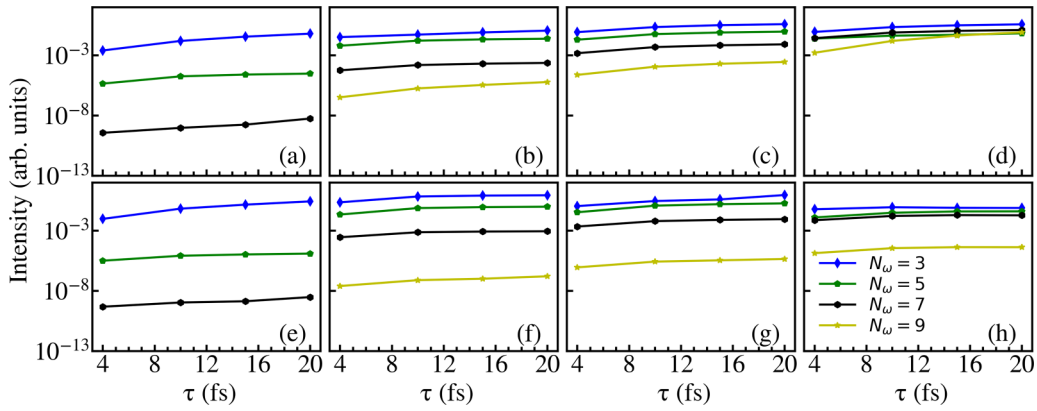
FIG. 8. Intensity of the first four high harmonics ($N_\omega = 3, 5, 7$, and 9) versus the relaxation time. The frequency of the pulse is $\hbar\omega_0 = 1$ eV in (a)–(d) and 2 eV in (e)–(h). The pulse amplitude is 0.1 V/Å (a),(e); 0.35 V/Å (b), (f), 0.5 V/Å (c), (g); and 0.75 V/Å (d), (h).

of the pulse $\hbar\omega_0 = 1$ eV, and relaxation time of 4 fs, the power radiated by the QD at frequency ω_0 is around 10 W/cm^2. Then, as follows from Figs. 6–8, the power radiated by the QD at the frequencies of high harmonics is a few orders of magnitude smaller.

One of the important characteristics of the radiation spectrum is its high harmonic cutoff, which is defined as the maximum harmonic order that can be generated during the pulse. In Fig. 9, the high harmonic cutoff is shown as a function of the pulse amplitude, F_0, for different frequencies of the pulse and different relaxation times. The curve for the relaxation time of 10 fs coincides with the one for $\tau = 4$ fs. When the relaxation time increases to 20 fs, then, as we mentioned above, the corresponding harmonic cutoff decreases. The dependence of the harmonic cutoff on the field amplitude is different for different frequencies of the pulse. For small frequency, $\hbar\omega_0 = 1$ eV, the dependence of the harmonic cutoff on F_0 is almost linear, see Fig. 9(a). The linear dependence of the HHG cutoff on the field amplitude is also observed in solids, both two-dimensional and three-dimensional [19].

Different behavior is observed for larger frequencies of the pulse, $\hbar\omega_0 = 2$ eV and 3.1 eV, see Figs. 9(b) and 9(c). In this case, there is a clear deviation from the linear dependence, namely, at small field amplitudes, $F_0 < 0.35$ V/Å, there is almost linear dependence of the harmonic cutoff on F_0, while at larger field amplitudes, $F_0 > 0.35$ V/Å, the harmonic cutoff becomes suppressed. Here, for the relaxation time of 20 fs, there is a saturation behavior and the harmonic cutoff

is constant, while for the smaller relaxation times, 4 fs and 10 fs, the harmonic cutoff is constant within a small range of F_0, up to 0.5 V/Å, and then it increases with the slope that is less then the one at small field amplitudes, $F_0 < 0.35$ V/Å.

When the frequency of the pulse becomes almost equal to the band gap, $\hbar\omega_0 = 3.1$ eV, the harmonic cutoff as the function of the field amplitude, see Fig. 9(c), also shows dependence with the variable slope. Here, the slope is large at small field amplitude, $F_0 < 0.1$ V/Å, then it decreases for $0.1 < F_0 < 0.35$ V/Å, becomes zero within some range of F_0, and increases again.

Thus, for the high frequencies of the pulse, $\hbar\omega_0 > 2$ eV, there is a suppression of the harmonic cutoff at large field amplitudes. Such a property can be attributed to a finite number of energy levels within graphene QD, which results in a finite energy range of around 16 eV, see Fig. 2. The harmonic cutoff in the HHG spectrum also determines the corresponding energy cutoff, which, for $\hbar\omega_0 = 2$ eV, is around 18 eV for the relaxation time of 20 fs and 26 eV for $\tau = 10$ fs. These values are larger than the QD energy range of 16 eV, which means that, at large field amplitude, the harmonic cutoff is determined by simultaneous transitions between many single-particle levels.

For all frequencies of the laser pulse, the harmonic cutoff is larger for the system with the smaller relaxation time, i.e., for the less coherent system. It is related to the fact that, for the coherent system, the electron dynamics is more reversible, see Fig. 4, which results in less population of the high-energy CB levels and correspondingly in smaller harmonic cutoff.

IV. CONCLUSION

Due to dimensional quantization, a graphene QD has an intrinsic band gap, which depends on the size of the dot. As a result, in the QD of a small size, an ultrafast electron dynamics in the field of a strong optical pulse can be both reversible and irreversible, depending on the frequency of the pulse. If the frequency of the pulse is much less than the band gap of the QD, then the electron dynamics is almost reversible, i.e., after the pulse, the electron system returns to its initial state. But if the frequency of the pulse is comparable to the band gap, then the electron dynamics is highly irreversible, i.e., the residual population of the excited QD states is almost the

FIG. 9. Harmonic cutoff versus the amplitude of the optical pulse. The frequency of the pulse is $\hbar\omega_0 = 1$ eV (a), 2 eV (b), and 3.1 eV (c). The relaxation time is shown next to the corresponding line in each panel. The first data point in all panels correspond to the field amplitude of 0.01 V/Å.

same as their maximum population during the pulse. The reversibility of electron dynamics is strongly affected by the dephasing processes. The dephasing processes make the electron dynamics incoherent and more irreversible. Since the electron dynamics completely determines the nonlinear optical response of the system, such as HHG, then the nonlinear optics of graphene QDs strongly depends on the dephasing processes.

The dephasing, which is introduced through relaxation of the nondiagonal elements of the density matrix, affects both the intensities of the high harmonics and the harmonic cutoff. With increasing the relaxation time, i.e., when the electron dynamics becomes more coherent, the intensities of harmonics increase. This can be attributed to the fact that for the coherent dynamics, more paths can contribute to formation of high harmonics coherently, resulting in larger intensity.

The effect of relaxation on the harmonic cutoff is also related to the reversibility of electron dynamics, namely, with increasing the relaxation time the electron dynamics becomes more reversible with less population of the highly excited QD levels. As a result, the harmonic cutoff decreases with increasing the relaxation time. As a function of the field amplitude, the harmonic cutoff shows almost linear dependence at small frequencies of the pulse when the corresponding energy cutoff is less than the energy range introduced by the lowest and highest energy levels in the QD. When this energy range becomes comparable to the energy cutoff, which happens at large frequencies of the pulse, then the cutoff shows a saturated behavior as a function of the pulse amplitude.

For experimental verification of the HHG from graphene QDs, an array of QDs should be prepared to enhance the intensity of the corresponding radiation. The measurements can be done following the standard experimental setup, where the emitted radiation is routed to a spectrometer [64]. An array of graphene QDs can also be used for generation of high-frequency optical pulses. Although the intensity of such pulses can be low, the pulses can be generated in the hard ultraviolet region.

[1] F. Krausz and M. Ivanov, Attosecond physics, Rev. Mod. Phys. **81**, 163 (2009).

[2] S. Y. Kruchinin, F. Krausz, and V. S. Yakovlev, Colloquium: Strong-field phenomena in periodic systems, Rev. Mod. Phys. **90**, 021002 (2018).

[3] A. Schiffrin, T. Paasch-Colberg, N. Karpowicz, V. Apalkov, D. Gerster, S. Muhlbrandt, M. Korbman, J. Reichert, M. Schultze, S. Holzner, J. V. Barth, R. Kienberger, R. Ernstorfer, V. S. Yakovlev, M. I. Stockman, and F. Krausz, Optical-field-induced current in dielectrics, Nature (London) **493**, 70 (2013).

[4] J. Kiemle, P. Zimmermann, A. W. Holleitner, and C. Kastl, Light-field and spin-orbit-driven currents in van der Waals materials, Nanophotonics **9**, 2693 (2020).

[5] T. Paasch-Colberg, A. Schiffrin, N. Karpowicz, S. Kruchinin, S. Ozge, S. Keiber, O. Razskazovskaya, S. Muhlbrandt, A. Alnaser, M. Kubel, V. Apalkov, D. Gerster, J. Reichert, T. Wittmann, J. V. Barth, M. I. Stockman, R. Ernstorfer, V. S. Yakovlev, R. Kienberger, and F. Krausz, Solid-state light-phase detector, Nat. Photonics **8**, 214 (2014).

[6] T. Higuchi, C. Heide, K. Ullmann, H. B. Weber, and P. Hommelhoff, Light-field-driven currents in graphene, Nature (London) **550**, 224 (2017).

[7] E. Gruber, R. A. Wilhelm, R. Pétuya, V. Smejkal, R. Kozubek, A. Hierzenberger, B. C. Bayer, I. Aldazabal, A. K. Kazansky, F. Libisch, A. V. Krasheninnikov, M. Schleberger, S. Facsko, A. G. Borisov, A. Arnau, and F. Aumayr, Ultrafast electronic response of graphene to a strong and localized electric field, Nat. Commun. **7**, 13948 (2016).

[8] S. Sederberg, D. Zimin, S. Keiber, F. Siegrist, M. S. Wismer, V. S. Yakovlev, I. Floss, C. Lemell, J. Burgdörfer, M. Schultze, F. Krausz, and N. Karpowicz, Attosecond optoelectronic field measurement in solids, Nat. Commun. **11**, 430 (2020).

[9] G. Vampa, J. Lu, Y. S. You, D. R. Baykusheva, M. Wu, H. Liu, K. J. Schafer, M. B. Gaarde, D. A. Reis, and S. Ghimire, Attosecond synchronization of extreme ultraviolet high harmonics from crystals, J. Phys. B: At., Mol. Opt. Phys. **53**, 144003 (2020).

[10] M. Trushin, A. Grupp, G. Soavi, A. Budweg, D. De Fazio, U. Sassi, A. Lombardo, A. C. Ferrari, W. Belzig, A. Leitenstorfer, and D. Brida, Ultrafast pseudospin dynamics in graphene, Phys. Rev. B **92**, 165429 (2015).

[11] S. A. Oliaei Motlagh, J.-S. Wu, V. Apalkov, and M. I. Stockman, Femtosecond valley polarization and topological resonances in transition metal dichalcogenides, Phys. Rev. B **98**, 081406(R) (2018).

[12] D. Sun, J.-W. Lai, J.-C. Ma, Q.-S. Wang, and J. Liu, Review of ultrafast spectroscopy studies of valley carrier dynamics in two-dimensional semiconducting transition metal dichalcogenides, Chin. Phys. B **26**, 037801 (2017).

[13] F. Gesuele, Ultrafast hyperspectral transient absorption spectroscopy: Application to single layer graphene, Photonics **6**, 95 (2019).

[14] J. Zhang, H. Ouyang, X. Zheng, J. You, R. Chen, T. Zhou, Y. Sui, Y. Liu, X. Cheng, and T. Jiang, Ultrafast saturable absorption of MoS_2 nanosheets under different pulse-width excitation conditions, Opt. Lett. **43**, 243 (2018).

[15] R. Boyd, *Nonlinear Optics*, 3rd ed. (Academic Press, Boston, MA, 2008).

[16] J. L. Krause, K. J. Schafer, and K. C. Kulander, High-Order Harmonic Generation from Atoms and Ions in the High Intensity Regime, Phys. Rev. Lett. **68**, 3535 (1992).

[17] D. von der Linde, T. Engers, G. Jenke, P. Agostini, G. Grillon, E. Nibbering, A. Mysyrowicz, and A. Antonetti, Generation of

high-order harmonics from solid surfaces by intense femtosecond laser pulses, Phys. Rev. A **52**, R25(R) (1995).

[18] P. A. Norreys, M. Zepf, S. Moustaizis, A. P. Fews, J. Zhang, P. Lee, M. Bakarezos, C. N. Danson, A. Dyson, P. Gibbon, P. Loukakos, D. Neely, F. N. Walsh, J. S. Wark, and A. E. Dangor, Efficient Extreme uv Harmonics Generated from Picosecond Laser Pulse Interactions with Solid Targets, Phys. Rev. Lett. **76**, 1832 (1996).

[19] S. Ghimire, A. D. DiChiara, E. Sistrunk, P. Agostini, L. F. DiMauro, and D. A. Reis, Observation of high-order harmonic generation in a bulk crystal, Nat. Phys. **7**, 138 (2011).

[20] G. Vampa, T. J. Hammond, N. Thiré, B. E. Schmidt, F. Légaré, C. R. McDonald, T. Brabec, and P. B. Corkum, Linking high harmonics from gases and solids, Nature (London) **522**, 462 (2015).

[21] G. Ndabashimiye, S. Ghimire, M. Wu, D. A. Browne, K. J. Schafer, M. B. Gaarde, and D. A. Reis, Solid-state harmonics beyond the atomic limit, Nature (London) **534**, 520 (2016).

[22] Y. L. Li, Y. S. You, S. Ghimire, T. F. Heinz, H. Z. Liu, and D. A. Reis, High-harmonic generation from an atomically thin semiconductor, Nat. Phys. **13**, 262 (2017).

[23] Y. Yin, Y. Wu, A. Chew, X. Ren, F. Zhuang, S. Gholam-Mirzaei, M. Chini, Z. Chang, Y. S. You, and S. Ghimire, High-harmonic generation in amorphous solids, Nat. Commun. **8**, 724 (2017).

[24] N. Klemke, N. Tancogne-Dejean, G. M. Rossi, Y. Yang, F. Scheiba, R. E. Mainz, G. Di Sciacca, A. Rubio, F. X. Kärtner, and O. D. Mücke, Polarization-state-resolved high-harmonic spectroscopy of solids, Nat. Commun. **10**, 1319 (2019).

[25] M. Lewenstein, P. Balcou, M. Y. Ivanov, A. L'Huillier, and P. B. Corkum, Theory of high-harmonic generation by low-frequency laser fields, Phys. Rev. A **49**, 2117 (1994).

[26] D. Golde, T. Meier, and S. W. Koch, High harmonics generated in semiconductor nanostructures by the coupled dynamics of optical inter- and intraband excitations, Phys. Rev. B **77**, 075330 (2008).

[27] N. Klemke, O. D. Mücke, A. Rubio, F. X. Kärtner, and N. Tancogne-Dejean, Role of intraband dynamics in the generation of circularly polarized high harmonics from solids, Phys. Rev. B **102**, 104308 (2020).

[28] I. Kilen, M. Kolesik, J. Hader, J. V. Moloney, U. Huttner, M. K. Hagen, and S. W. Koch, Propagation Induced Dephasing in Semiconductor High-Harmonic Generation, Phys. Rev. Lett. **125**, 083901 (2020).

[29] Z. Xie, F. Zhang, Z. Liang, T. Fan, Z. Li, X. Jiang, H. Chen, J. Li, and H. Zhang, Revealing of the ultrafast third-order nonlinear optical response and enabled photonic application in two-dimensional tin sulfide, Photonics Res. **7**, 494 (2019).

[30] L. Lu, W. Wang, L. Wu, X. Jiang, Y. Xiang, J. Li, D. Fan, and H. Zhang, All-optical switching of two continuous waves in few layer bismuthene based on spatial cross-phase modulation, ACS Photonics **4**, 2852 (2017).

[31] L. Wu, Y. Dong, J. Zhao, D. Ma, W. Huang, Y. Zhang, Y. Wang, X. Jiang, Y. Xiang, J. Li, Y. Feng, J. Xu, and H. Zhang, Kerr nonlinearity in 2D graphdiyne for passive photonic diodes, Adv. Mater. **31**, 1807981 (2019).

[32] L. Gao, C. Li, W. Huang, S. Mei, H. Lin, Q. Ou, Y. Zhang, J. Guo, F. Zhang, S. Xu, and H. Zhang, MXene/polymer membranes: Synthesis, properties, and emerging applications, Chem. Mater. **32**, 1703 (2020).

[33] R. C. Ashoori, Electrons in artificial atoms, Nature (London) **379**, 413 (1996).

[34] T. Chakraborty, in *Quantum Dots* (Elsevier, Amsterdam, Netherlands, 1999).

[35] Y. Arakawa and H. Sakaki, Multidimensional quantum well laser and temperature dependence of its threshold current, Appl. Phys. Lett. **40**, 939 (1982).

[36] D. Loss and D. P. DiVincenzo, Quantum computation with quantum dots, Phys. Rev. A **57**, 120 (1998).

[37] X. Michalet, F. F. Pinaud, L. A. Bentolila, J. M. Tsay, S. Doose, J. J. Li, G. Sundaresan, A. M. Wu, S. S. Gambhir, and S. Weiss, Quantum dots for live cells, in vivo imaging, and diagnostics, Science (New York, N.Y.) **307**, 538 (2005).

[38] V. Veeramani, Z. Bao, M.-H. Chan, H.-C. Wang, A. Jena, H. Chang, S.-F. Hu, and R.-S. Liu, Quantum dots for light conversion, therapeutic and energy storage applications, J. Solid State Chem. **270**, 71 (2019).

[39] Q. Liu, J. Sun, K. Gao, N. Chen, X. Sun, D. Ti, C. Bai, R. Cui, and L. Qu, Graphene quantum dots for energy storage and conversion: From fabrication to applications, Mater. Chem. Front. **4**, 421 (2020).

[40] K. K. Hansen, D. Bauer, and L. B. Madsen, Finite-system effects on high-order harmonic generation: From atoms to solids, Phys. Rev. A **97**, 043424 (2018).

[41] D. Pan, J. Zhang, Z. Li, and M. Wu, Hydrothermal route for cutting graphene sheets into blue-luminescent graphene quantum dots, Adv. Mater. **22**, 734 (2010).

[42] S. Chung, R. A. Revia, and M. Zhang, Graphene quantum dots and their applications in bioimaging, biosensing, and therapy, Adv. Mater. **33**, 1904362 (2021).

[43] H. Sun, L. Wu, W. Wei, and X. Qu, Recent advances in graphene quantum dots for sensing, Mater. Today **16**, 433 (2013).

[44] M. Bacon, S. J. Bradley, and T. Nann, Graphene quantum dots, Part. Part. Syst. Charact. **31**, 415 (2014).

[45] K. S. Novoselov, A. K. Geim, S. V. Morozov, D. Jiang, Y. Zhang, S. V. Dubonos, I. V. Grigorieva, and A. A. Firsov, Electric field effect in atomically thin carbon films, Science **306**, 666 (2004).

[46] A. K. Geim and K. S. Novoselov, The rise of graphene, Nat. Mater. **6**, 183 (2007).

[47] A. H. Castro Neto, F. Guinea, N. M. R. Peres, K. S. Novoselov, and A. K. Geim, The electronic properties of graphene, Rev. Mod. Phys. **81**, 109 (2009).

[48] D. S. L. Abergel, V. Apalkov, J. Berashevich, K. Ziegler, and T. Chakraborty, Properties of graphene: A theoretical perspective, Adv. Phys. **59**, 261 (2010).

[49] S. Das Sarma, S. Adam, E. H. Hwang, and E. Rossi, Electronic transport in two-dimensional graphene, Rev. Mod. Phys. **83**, 407 (2011).

[50] A. F. Young and P. Kim, Electronic transport in graphene heterostructures, Annu. Rev. Condens. Matter Phys. **2**, 101 (2011).

[51] H. K. Kelardeh, V. Apalkov, and M. I. Stockman, Graphene in ultrafast and superstrong laser fields, Phys. Rev. B **91**, 045439 (2015).

[52] S. A. Oliaei Motlagh, F. Nematollahi, V. Apalkov, and M. I. Stockman, Topological resonance and single-optical-cycle valley polarization in gapped graphene, Phys. Rev. B **100**, 115431 (2019).

[53] S. A. Oliaei Motlagh and V. Apalkov, Absorption properties of graphene quantum dots under ultrashort optical pulses, Phys. Rev. B **104**, 045421 (2021).

[54] S. J. Hossaini, R. Ghimire, and V. Apalkov, Ultrafast nonlinear absorption of tmdc quantum dots, Physica E **142**, 115239 (2022).

[55] L. D. Landau and E. M. Lifshitz, *Quantum Mechanics: Non-relativistic Theory*, Vol. 3 (Elsevier, Amsterdam, 2013).

[56] K. Blum, *Density Matrix Theory and Applications*, Vol. 64 (Springer Science & Business Media, Berlin, 2012).

[57] P. R. Wallace, The band theory of graphite, Phys. Rev. **71**, 622 (1947).

[58] R. Saito, G. Dresselhaus, and M. Dresselhaus, *Physical Properties of Carbon Nanotubes* (Imperial College Press, London, 1998).

[59] K. Ahnert and M. Mulansky, Odeint—solving ordinary differential equations in C++, AIP Conf. Proc. **1389**, 1586 (2011).

[60] Z.-Y. Chen and R. Qin, High harmonic generation in graphene–boron nitride heterostructures, J. Mater. Chem. C **8**, 12085 (2020).

[61] G. Vampa, C. R. McDonald, G. Orlando, P. B. Corkum, and T. Brabec, Semiclassical analysis of high harmonic generation in bulk crystals, Phys. Rev. B **91**, 064302 (2015).

[62] Y. W. Kim, T.-J. Shao, H. Kim, S. Han, S. Kim, M. Ciappina, X.-B. Bian, and S.-W. Kim, Spectral interference in high harmonic generation from solids, ACS Photonics **6**, 851 (2019).

[63] M. Ivanov and O. Smirnova, Opportunities for sub-laser-cycle spectroscopy in condensed phase, Chem. Phys. **414**, 3 (2013).

[64] E. Goulielmakis and T. Brabec, High harmonic generation in condensed matter, Nat. Photonics **16**, 411 (2022).